An Improved Parameter-free Waveform Controller for Fast and Accurate Measurement of the Magnetic Properties of Grain-oriented Electrical Steels

Long Chen^{1,2,3}, Hainan Huang¹, Tong Ben^{1,2*}, Biao Huang¹, and XianZhi Liu¹

¹College of Electrical Engineering and New Energy, China Three Gorges University, Yichang 443002, Hubei Province, China
²Hubei Provincial Research Center on Microgrid Engineering Technology (China Three Gorges University),
Yichang 443002, Hubei Province, China

³Hubei Provincial Engineering Technology Research Center for Power Transmission Line, China Three Gorges University, Yichang, 443002, China

(Received 9 May 2025, Received in final form 3 September 2025, Accepted 4 September 2025)

To address nonlinearity-induced waveform distortion and slow convergence in the magnetic characterization of electrical steels, a parameter-free controller is proposed in this work, which enhances convergence speed while maintaining tracking accuracy and avoiding parameter dependence via adaptive compensation mechanisms. The controller consists of two primary components: the first incorporates polynomial fitting for rapid evaluation, which considerably reduces the number of iterations; the second employs a strategy that decouples frequency-domain and time-domain control. This strategy initially normalizes the waveform, then independently modulates its amplitude and shape, thus enabling rapid and precise waveform control. The controller has been successfully implemented in three one-dimensional (1-D) magnetic measurement systems. The results demonstrate that through assessment of the initial excitation in magnetic measurements of grain-oriented silicon steel, the initial waveform error is reduced to less than 3%, the harmonic content of the final waveform is controlled to approximately 0.2%, and the root mean square error of the waveform is maintained below 0.5%. Furthermore, magnetic property measurements were conducted over a frequency range from 2 Hz to 2000 Hz, with multiple loss values obtained at different frequencies for uncertainty analysis.

Keywords: electrical steels, magnetic properties measurement, hysteresis loops, adaptive controller

1. Introduction

The characterization of magnetic properties in electrical steels involves the precise determination of magnetization curves, permeability, saturation magnetization, coercivity, and other relevant parameters [1]. The performance of electromagnetic devices, such as transformers, inductors, and motors, is critically dependent on the magnetic properties of the materials used. Accurate measurement of these properties is essential for gaining critical insights into the behavior of electrical steels, thereby forming the foundation for the optimization of electromagnetic device design and fabrication [2-5]. International standards mandate that power loss measurements be conducted under a sinusoidal magnetic flux density waveform to ensure the repeatability and reproducibility of the results

[6]. Due to the inherent design of the testing equipment and the nonlinear behavior of electrical steels, distortion of the magnetic flux density waveform is inevitable during the measurement process, leading to waveforms that fail to meet the international standards for loss measurement [7]. Moreover, measurement duration, especially at extremely low or high frequencies, can be considerably prolonged as a result of exacerbated waveform distortion. Prolonged measurement time may induce additional thermal effects in the electrical steels, which can further degrade the accuracy of loss measurements [8, 9]. Therefore, a feedback control mechanism is necessary to rapidly correct the magnetic flux density waveform and ensure compliance with standardized measurement requirements.

At the current state of the art, various controllers have been developed to achieve a standard sinusoidal magnetic flux density waveform [10], which are broadly categorized into digital and analog control methods. In Ref. [11, 12],

©The Korean Magnetics Society. All rights reserved.

*Corresponding author: Tel: +86 13820296113

e-mail: bentong@ctgu.edu.cn

an analog controller is used to adjust the magnetic flux density signal in real time, offering high-speed control but exhibiting inadequate stability in high-frequency applications. With the fast development of advanced data acquisition (DAQ) techniques, analog controllers have been largely superseded by digital controllers. Various digital control strategies have been explored to enhance convergence speed and accuracy. In Ref. [13, 14], the flux density waveform is controlled in the time domain using a classical proportional-integral (PI) controller, which is valued for its structural simplicity. However, this method requires numerous iterations to achieve waveform control under nonlinear conditions. Additionally, distinct control parameters are necessary for different materials, and these parameters are not easily determined. To address this challenge, a parameter-free adaptive controller has been introduced, as described in [15, 16]. It is reported that this method eliminates the need for additional parameter configuration and supports a faster control process. Nevertheless, both control strategies utilize waveformminus-waveform techniques, which are prone to introducing measurement noise (e.g., Gaussian white noise and power supply oscillations) into the feedback loop, especially during low-frequency magnetic property measurements. To overcome the shortcomings of time domain control, some researchers try to control the waveform in the frequency domain. In frequency-domain control, the amplitude and phase of the waveform, derived through Fourier decomposition, are independently controlled using a PI controller, effectively suppressing harmonic components in the waveform, as noted in [17]. However, this method introduces additional system complexity since four extra control parameters must be configured. Moreover, these control parameters are empirically established and remain fixed during the control process, making it difficult to adjust them promptly in response to the complex variations encountered in the waveform control process. Consequently, overshooting is prone to occur, resulting in an increased number of control system iterations, which compromises system stability and induces oscillations. To further improve the stability of the control process and accelerate the convergence speed, neural networks (NN) have been incorporated into the control strategy in recent years [18, 19]. This approach demonstrates remarkable advantages by achieving control performance that meets established criteria within a limited number of iterations. Nonetheless, the implementation of this approach is heavily dependent on a substantial volume of preexisting test results to serve as the training dataset, a prerequisite for its application. In addition, when dealing with different types of silicon steel sheets, the neural network model needs to undergo time-consuming retraining to adapt to their unique material properties. Consequently, despite this method's considerable potential in control efficacy, the initial tasks of data preparation and model training are arduous and time-consuming. This limitation is similar to control strategies based on tester modeling, as both require extensive preliminary work to determine the characteristic parameters of the device for model construction, as described in detail in [20-22]. In summary, current digital controllers still struggle to simultaneously meet the demand for rapid convergence speed and high control accuracy.

To address the aforementioned issues, an improved parameter-free control scheme is proposed in this paper to overcome the challenges of slow convergence and suboptimal control performance in waveform control during magnetic property measurements. In the proposed method, a polynomial is constructed to evaluate the initial excitation voltage waveform, thereby enabling the controller to effectively guide the controlled waveform toward the target waveform and significantly reduce the number of intermediate iterations. Moreover, the controlled waveform is decomposed into two components: amplitude and normalized waveform. These components are adaptively controlled in both the time and frequency domains, which effectively suppresses high-frequency harmonic distortions. Notably, all necessary control parameters are computed automatically. The proposed algorithm was evaluated on a Grain-Oriented (GO) electrical steel measurement system operating in the frequency range from 2 Hz to 2000 Hz. To demonstrate its adaptability, experiments were conducted over various frequency bands using a Single Sheet Tester (SST), a Ring Core Sample (RCS), and an Epstein Frame (EF).

2. Measurement Systems and Controllers

2.1. Measurement systems

To assess the controller's performance, a magnetic measurement system incorporating digital feedback was constructed, as illustrated in Fig. 1. This system consisted of an NI DAQ card, a power amplifier, an SST, an RCS, an EF, and a preamplifier SR560. The test specimens were thin laminations or toroidal cores made of grain-oriented silicon steel. In the experimental setup, a 16-bit DAQ card was employed to generate the magnetization waveform, which was then amplified through a power amplifier and supplied to the excitation coil to magnetize the test specimens. The induced voltage $V_{\rm get}(t)$ and the excitation current $I_{\rm mag}(t)$ were first attenuated using high-

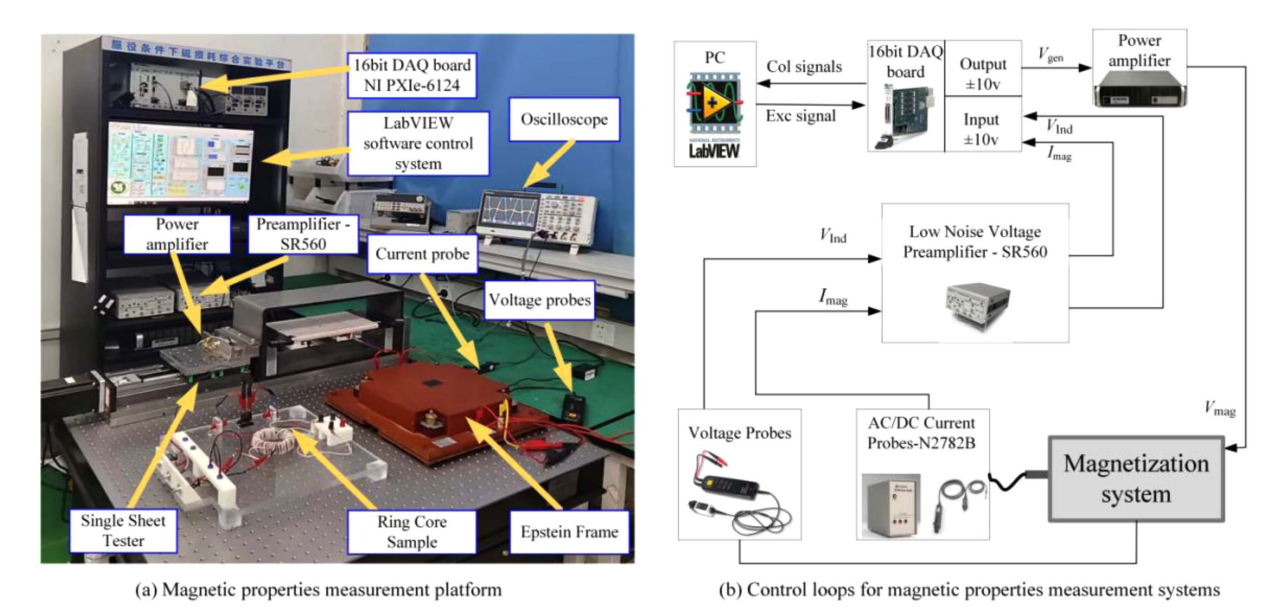


Fig. 1. (Color online) Measuring system for magnetic properties of electrical steel.

precision voltage and current probes. Subsequently, these signals were processed by a low-noise preamplifier (SR560) to suppress noise and improve the signal-to-noise ratio. The conditioned signals were then fed back to the DAQ card for further processing. Using LabVIEW software, the acquired signals were processed and subsequently transformed into the frequency domain through Fast Fourier Transform (FFT) for the extraction of frequency components. The magnetic flux density B(t)

was iteratively refined to align with the target reference value $B_{ref}(t)$. The magnetic flux density B(t) and the magnetic field strength H(t) of the specimen were calculated using the following equations:

$$\begin{cases}
B(t) = -\frac{1}{N_2 S_{\text{sam}}} \int_0^t v_{\text{get}}(t) dt + (\frac{S_{\text{coi}}}{S_{\text{sam}}} - 1) \mu_0 H(t) \\
H(t) = \frac{N_1}{L_e} i_{\text{mag}}(t)
\end{cases}$$
(1)

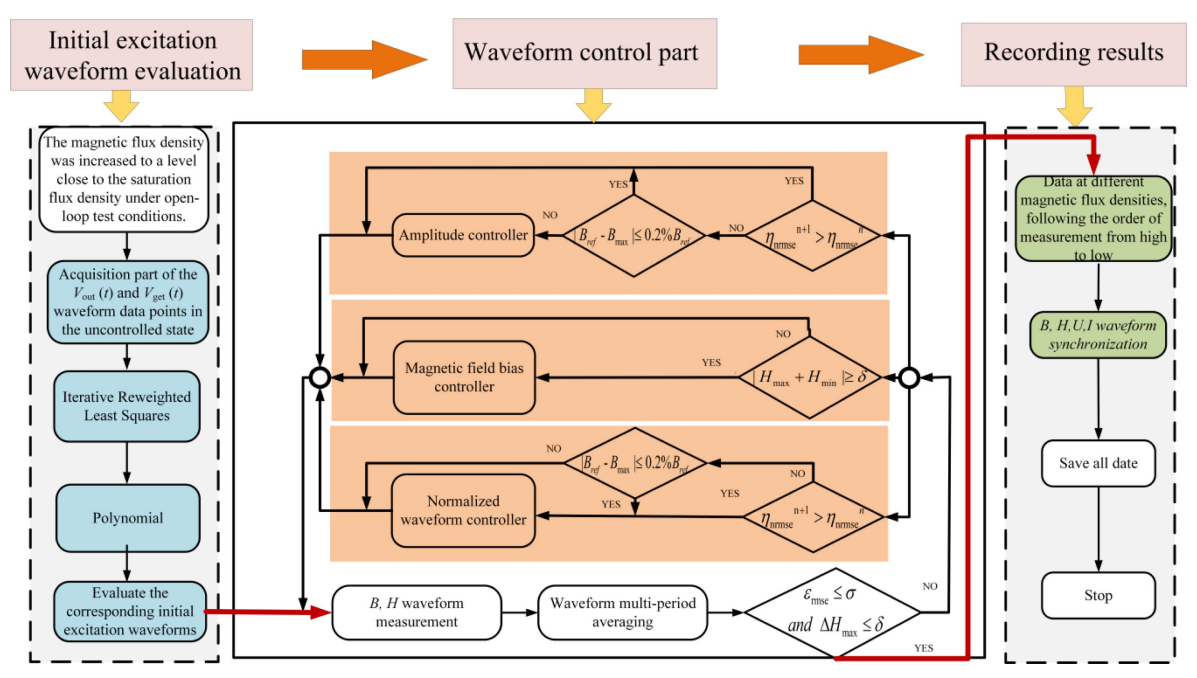


Fig. 2. (Color online) Modular architecture of the control algorithm and data flow diagram.

Where N_1 and N_2 denote the number of turns of the excitation and induction coils, respectively, $S_{\rm coi}$ represents the cross-sectional area of the induction coil, $S_{\rm sam}$ is the cross-sectional area of the sample, $L_{\rm e}$ indicates the average magnetic path length of the measurement device, and μ_0 is the vacuum permeability.

2.2. Principle of the controller

The control strategy employed by the controller is illustrated in Fig. 2. It comprises three distinct components: initial excitation waveform evaluation, waveform control, and the processing and recording of experimental data. In the initial stage of magnetization assessment, the magnetic flux density is first increased to the saturation level under open-loop test conditions; a polynomial model is established based on the excitation voltage and the induced voltage waveforms, allowing the magnetic induction signal to converge rapidly to the preset target waveform. Subsequently, a three-loop control strategy for waveform regulation is employed by the system. First, the multi-cycle B-H waveform is subjected to cyclic averaging to suppress random noise and enhance the signal-to-noise ratio. Then, the waveform is decomposed into three components: its amplitude, a normalized waveform shape, and a DC bias component. The timedomain controller regulates the amplitude of the excitation, whereas the FFT-based frequency-domain controller suppresses harmonic distortions and corrects phase deviations; the DC bias is independently compensated for. The controller optimizes iteratively, prioritizing amplitude optimization over waveform optimization, and then recombines to generate a new excitation waveform. Once the B-H waveform meets the predefined precision criteria, the control process is terminated, which subsequently initiates the synchronous acquisition and recording of the final waveform data. The indicators used to characterize waveform quality include the normalized waveform root mean square error η_{nrmse} and the waveform root mean square error $\varepsilon_{\rm rmse}$, which are defined as follows:

$$\eta_{nrmse} = \sqrt{\frac{\int [b_{ref}(t) - b_{get}(t)]^2 dt}{n}}$$
 (2)

$$\varepsilon_{\text{rmse}} = \sqrt{\frac{\int [B_{\text{ref}}(t) - B_{\text{get}}(t)]^2 dt}{\int B_{\text{ref}}(t)^2 dt}}$$
(3)

Where n is the number of sampling points for each signal cycle. $b_{\text{ref}}(t)$ is the normalized reference waveform. $B_{\text{get}}(t)$ corresponds to the measured time-domain signal of magnetic flux density, whereas $b_{\text{get}}(t)$ refers to its

normalized waveform following amplitude normalization.

2.2.1. Initial excitation voltage waveform evaluation

In the first phase, during the evaluation of the initial excitation voltage waveform, a polynomial model was established to accelerate convergence. An iterative reweighted least squares (IRLS) method was proposed to construct a polynomial model to approximate the measurement system's nonlinear characteristics. This method iteratively optimizes the model parameters to minimize the residual sum of squares. Specifically, the excitation signal $V_{\rm out}(t)$ and the induced signal $V_{\rm get}(t)$ were represented as vectors B and A, respectively, with the coefficients to be fitted denoted as X:

$$A = \begin{bmatrix} V_{\text{get},1} & V_{\text{get},1} & \dots & V_{\text{get},1} \\ V_{\text{get},2} & V_{\text{get},2} & \dots & V_{\text{get},2} \\ \vdots & \vdots & \ddots & \vdots \\ V_{\text{get},n} & V_{\text{get},n} & \dots & V_{\text{get},n} \end{bmatrix} \quad B = \begin{bmatrix} V_{\text{out},1} \\ V_{\text{out},2} \\ \vdots \\ V_{\text{out,n}} \end{bmatrix} \quad X = \begin{bmatrix} a_0 \\ a_1 \\ \vdots \\ a_j \end{bmatrix}$$
(4)

Where n represents the number of points collected in a single cycle, and j represents the polynomial order. $V_{\rm get}(t)$ and $V_{\rm out}(t)$ are the corresponding induced and excitation voltage waveforms for the initial magnetization and saturation magnetization phases captured during the open-loop test. To achieve a superior approximation of the nonlinear system with the polynomial model, the fitting coefficients require iterative optimization, which is accomplished by updating the parameters according to Eq. (5):

$$X^{(t+1)} = \arg_{X} \min \sum_{i=1}^{n} \frac{|B - A_{i}X|^{2}}{\max \left\{ \delta, |B - A_{i}X^{(t)}| \right\}}$$
 (5)

Where δ a small value, in this case, is 0.0001, which mainly avoids division by zero. After the key coefficients have been solved, a polynomial can be constructed to approximate the magnetic properties measurement system in the following form:

$$V_{out} = f(V_{ref}) = a_0 + a_1 V_{ref}^1 + a_2 V_{ref}^2 \cdots + a_n V_{ref}^n$$
 (6)

Where V_{ref} is derived from the reference magnetic flux density, which is expressed as:

$$V_{\text{ref}}(t) = -N_2 S_{coi} \frac{dB_{\text{ref}}(t)}{dt}$$
 (7)

By substituting the reference voltage waveform obtained from Equation (7) into the fitted polynomial, the initial excitation voltage waveform can then be evaluated:

$$B = AX \tag{8}$$

This method facilitates the determination of the initial excitation voltage waveform, eliminating or significantly reducing the need for further iterations within the linear region. In the non-linear region, only a small number of iterations are required to satisfy the control requirements. The polynomial fitting is performed rapidly, allowing for the efficient evaluation of the initial excitation across various magnetic flux densities without intermediate transition iterations.

2.2.2. Waveform control part

Since the initial magnetic flux density waveform derived from the excitation evaluation deviated from the reference waveform, iterative adjustments to the excitation signal were necessary. Specifically, the waveform amplitude, the normalized waveform, and the DC bias obtained from the decomposition require further precise control.

(a) Amplitude control loop

Adopting a strategy of prioritizing amplitude adjustment over normalized waveform adjustment, the controller initially regulates the deviated amplitude to within the preset range. However, it is difficult for traditional proportional controllers to meet the control requirements within an acceptable number of iterations, which can be described as follows:

$$|V_{out}(t)^{(i+1)}| = |V_{out}(t)^{(i)}| + K_p \cdot |e(n)| + K_i |\sum_{i=0}^n e(n)|$$
 (9)

Where e(n) is the current iteration error, K_P and K_i represent the proportional and integral coefficients,

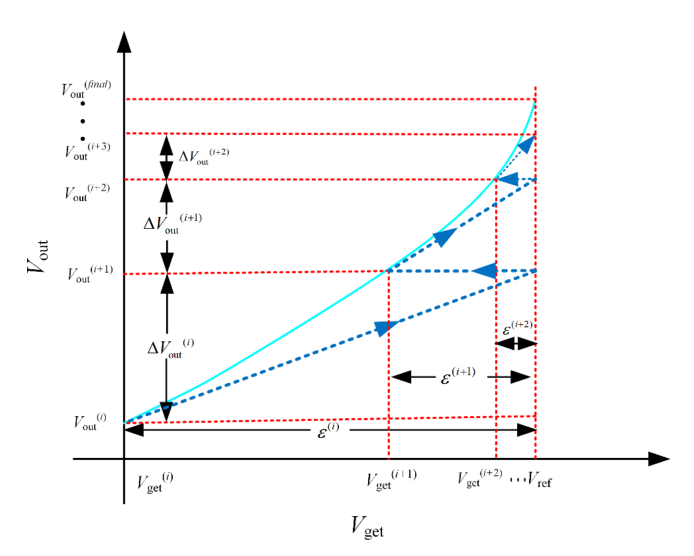


Fig. 3. (Color online) Relationship between the excitation voltage peak and the induced voltage peak in a polynomial.

respectively. The stability and rapid convergence time of the controller depend on the appropriate configuration of these parameters, a notably challenging task. As illustrated in Fig. 3, the polynomial approximation characterizes the relationship between the excitation voltage and the induced output of the measurement system. A novel approach is proposed to suppress the error ε between the measured amplitude $V_{\rm get}$ and the target amplitude $V_{\rm ref}$. The first derivative of the polynomial function (4) at the current measured voltage is utilized as a dynamic compensation coefficient. This method enables dynamic compensation for $V_{\rm get}$ by incorporating the extracted coefficient, which establishes a rapid error convergence mechanism in the time domain and significantly enhances the system's tracking speed toward V_{ref} . The specific mathematical formulation of this algorithm is expressed as follows:

$$|V_{\text{out}}(t)^{(i+1)}| = |V_{\text{out}}(t)^{(i)}| + \frac{K_{\text{M}}^{(i+1)}}{G} (|V_{\text{ref}}(t)| - |V_{\text{get}}(t)^{(i+1)}|)$$
with $K_{\text{M}}^{(i+1)} = \frac{\mathrm{d}f(|V_{\text{get}}^{(i+1)}|)}{\mathrm{d}V_{\text{get}}}$ (10)

By mathematical derivation, equation (10) can be reformulated in the following form:

$$|V_{\text{out}}(t)^{(i+1)}| = |V_{\text{out}}(t)^{(i)}| + \frac{2\pi}{G} N_2 S_{\text{coi}} K_M(|B_{\text{ref}}| - |B_{\text{get}}^{(i+1)}|)$$
 (11)

Where G is the power amplifier gain multiplier, and f is the test frequency.

(b) Normalized waveform control loop

Once the waveform amplitude control has met the preset requirements or severe waveform distortion has occurred, it is necessary to adjust its normalized waveform. In normalized waveform control, distortion arises primarily from incorporating numerous odd harmonics in regions of high magnetic flux density, exacerbated by noise. Traditional methods, which involve extensive point-by-point calculations of the time-domain waveform in numerical implementations, unintentionally introduce measurement noise into the computational process. This results in unsatisfactory control outcomes and increases the iteration count. To address these issues and mitigate high-frequency noise, the concept of frequency-domain control is integrated into the waveform control loop. To regulate the flux density waveform towards a sinusoidal profile, specific harmonic components (e.g., 3rd, 5th, and 7th orders) matching the harmonic frequencies and phases with inverted amplitudes must be strategically injected into the excitation signal to counteract the inherent harmonic distortion. The frequency domain control is applied to a normalized waveform derived via transformation rather than directly to the waveform's amplitude and phase. In this method, the reference waveform $V_{\text{ref}}(t)$ is separated into amplitude and normalized waveform components, which can be expressed as:

$$V_{\text{ref}}(t) = V_{\text{ref}} \cdot v_{\text{ref}}(t) \tag{12}$$

According to the Fast Fourier Transform (FFT), the normalized waveform can be expressed as:

$$v_{\text{ref}}(t) = \sum_{k=1}^{n} \left[a_{\text{ref},k} \cdot \cos\left(k \cdot 2\pi f t + \varphi_{\text{ref},k}\right) \right]$$
 (13)

Where $a_{\rm ref,k}$ is the amplitude of the kth harmonic, k is the odd harmonic number, and $\varphi_{\rm ref,k}$ is the phase of the kth harmonic. The collected $V_{\rm get}(t)$ was converted using the same method. During the iterative optimization process, the normalized excitation waveform was adjusted through harmonic injection while maintaining a constant amplitude, whereby harmonic components were compensated via $K_{\rm M}$ parameters. Experimental results demonstrated good convergence characteristics, and the iterative process was expressed as :

$$v_{out}(t)^{(i+1)} = v_{out}(t)^{(i)} + \sum_{k=1}^{n} \left[K_{M}^{(i+1)} \left(a_{\text{ref,k}} - a_{\text{get,k}}^{(i+1)} \right) \cdot \cos \left(k \cdot 2\pi ft + \varphi_{\text{get,k}}^{(i+1)} \right) \right] (14)$$

Where $a_{\text{get,k}}$ is the measured amplitude of the kth harmonic, k is the number of odd harmonics, and $\varphi_{\text{get,k}}$ is the measured phase of the kth harmonic.

(c) Magnetic field compensation control loop

Magnetic field offsets are inevitably introduced by factors such as the Earth's magnetic field and the output bias of power amplifiers. In the absence of a DC offset, the waveform would exhibit perfect symmetry. Although the negative feedback algorithm can suppress harmonic components in the output waveform, the DC bias persistently remains in the magnetizing current. Consequently, the acquired magnetic hysteresis loop demonstrates an inherent asymmetry about the origin. By introducing a suitable offset into the output waveform, the rate at which the magnetic field offset changes with the voltage offset is then calculated. Subsequently, the DC deviation in the magnetic field strength is eliminated through several iterations, with the iterative expression provided in Equation (15):

$$V_{\text{off}}^{(i+1)} = V_{\text{off}}^{(i)} + \frac{dV_{\text{off}}}{dH_{\text{off}}} \left(\frac{H_{\text{max}} - H_{\text{min}}}{2} \right)$$
 (15)

Where $V_{\rm off}$ is the offset voltage used for correction, $H_{\rm max}$ and $H_{\rm min}$ are the maximum and minimum values of the magnetic field strength, respectively.

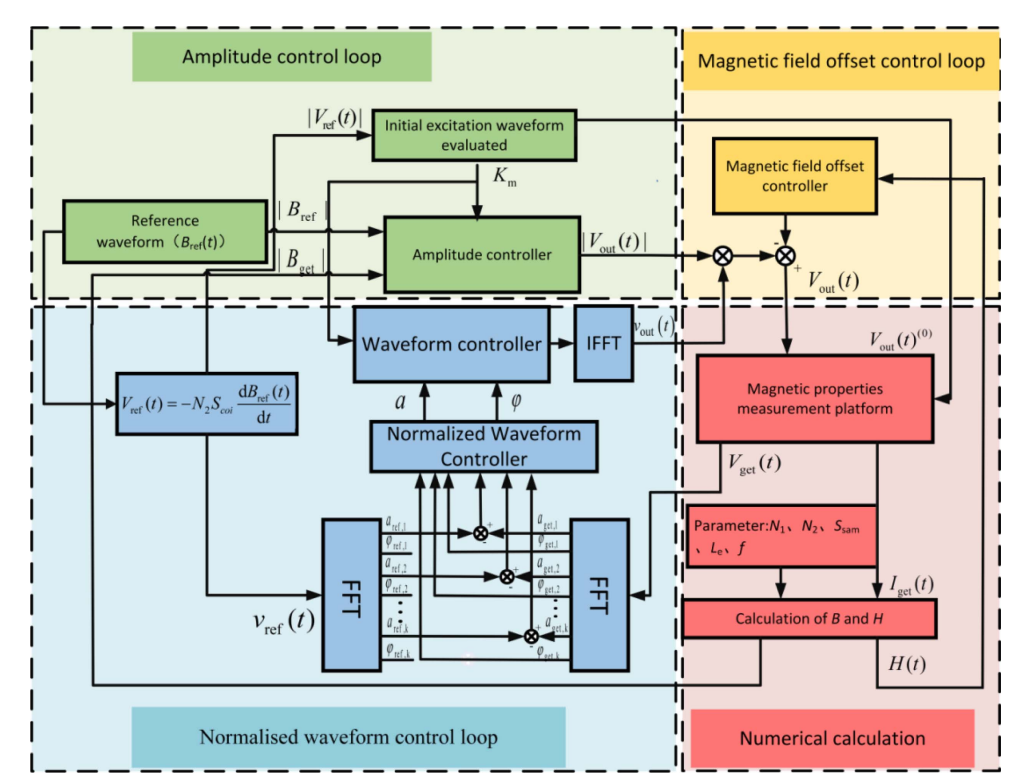


Fig. 4. (Color online) Block diagram of the program running in LabVIEW.

In summary, the controller controls the above three parts independently during each iteration and ultimately integrates them to produce the output. The iterative expression utilized for this process is as follows:

$$V_{\text{out}}(t)^{(i+1)} = |V_{\text{out}}(t)^{(i)}| \cdot v_{\text{out}}(t)^{(i)} + V_{\text{off}}^{(i)}$$
(16)

3. Controller Implementation

The control algorithm for the entire measurement system is implemented using the NI multifunctional data acquisition card PXIe-6124 within the LabVIEW platform. Fig. 4 illustrates the primary workflow that elaborates the operational mechanism of the controller system. Specifically, control parameters derived from the polynomial fitting algorithm are applied to the amplitude and waveform controller to achieve rapid waveform conditioning. Simultaneously, the integrated magnetic field bias controller conducts real-time monitoring of magnetic field deviations and implements closed-loop compensation. It should be noted that the three control loops in the waveform control system are not in a permanently active state but adaptively adjusted according to different conditions. The following describes the conditions under which the three control loops stop operation.

In the amplitude control loop:

1) When $\eta_{\text{nrmse}}^{(n+1)} > \eta_{\text{nrmse}}^{(n)}$, the waveform distortion is severe, and the waveform control loop is needed to

improve η_{nrmse} .

- 2) When $|B_{\text{get, max}}-B_{\text{ref, max}}| < 0.2\%B_{\text{ref,max}}$, the amplitude control loop meets the control requirement;
- 3) When ε_{rmse} is less than or equal to the required value. In the normalized waveform control loop:
- 1) When η_{nrmse} is less than or equal to the required value
- 2) The amplitude control loop does not meet control requirements.
 - 3) When $\varepsilon_{\rm rmse}$ is less than or equal to the required value. In the magnetic field compensation control loop:
 - 1) When $|H_{\text{max}} + H_{\text{min}}|$ is less than the required value.

4. Results and Discussion

To validate the effectiveness of the proposed algorithm, the controller's performance was comprehensively evaluated using three types of testers (SST, RCS, and EF) under sinusoidal excitation across a frequency range of 2 Hz to 2000 Hz. The analysis, which was focused on the controller's precision, speed, stability, and applicability, demonstrated its overall performance. Table 1 provides detailed reference information, including the specific dimensions of the test materials.

4.1. Evaluation and analysis of controller convergence speed

The rapid response characteristic of the controller is demonstrated through the initial excitation evaluation

Table 1. Details table of material specifications for different testers.

Testing apparatus	Material Type	Dimensions (mm)	
SST	Grain-oriented SiFe (B30P105/30JQ130)	Length: 500, Width: 170, Thickness: 0.3	
RCS	Grain-oriented SiFe (B30P105)	Outer diameter: 100, Inner diameter: 80, Height: 20	
EF	Grain-oriented SiFe (B30P105/30JQ130)	Length: 300, Width: 30, Thickness: 0.3	

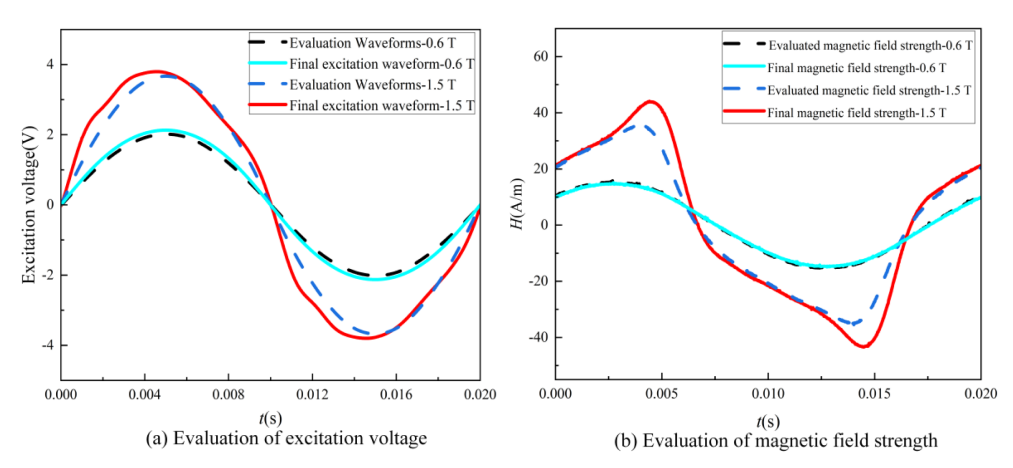


Fig. 5. (Color online) Evaluation results of the polynomial model in the linear region as well as in the nonlinear region.

method, which substantially accelerates the control process. As shown in Fig. 5, within the linear region, the excitation voltage and magnetic field waveforms generated by the polynomial model closely match the final waveforms obtained after multiple iterations. This phenomenon indicates that within this linear region, the controller exhibits high evaluation accuracy, which requires minimal iteration steps to satisfy the control criteria. In the nonlinear region, although the initial waveform estimation does not precisely coincide with the final iterative waveform, the discrepancy is significantly reduced. Nonetheless, the initial waveform estimation can still effectively reduce unnecessary intermediate iterative steps, thereby improving the measurement efficiency.

Following initial waveform estimation, further waveform optimization is required to satisfy the control specifications. Fig. 6 displays the waveforms of $V_{\rm get}(t)$ and H(t) during the excitation iteration process, highlighting the

changes in the induced voltage and magnetic field strength. The controller operates by prioritizing amplitude control before adjusting the normalized waveform. The region marked by the purple arrow corresponds to the amplitude control stage. During this stage, only the amplitude of the excitation signal is modulated, while the normalized waveform remains unaltered. As a result, the amplitude of the induced waveform changes, but the overall waveform does not change significantly, as evidenced by the variations in the height of the waveform peaks and troughs. In contrast, the cyan part represents the waveform shape control stage, during which the shape and phase of the induced waveform undergo significant changes due to the injection of specific harmonics while the amplitude remains essentially constant.

The convergence characteristics of the controller's $\varepsilon_{\rm rmse}$ under various excitation frequencies are exhibited, alongside a comparative analysis with conventional controllers,

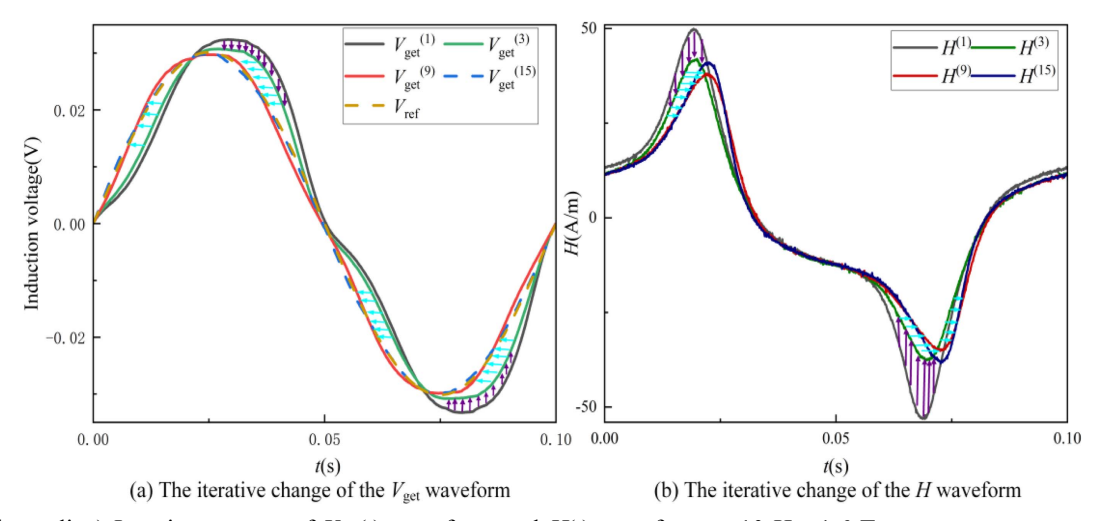


Fig. 6. (Color online) Iterative process of $V_{get}(t)$ waveform and H(t) waveform at 10 Hz, 1.6 T.

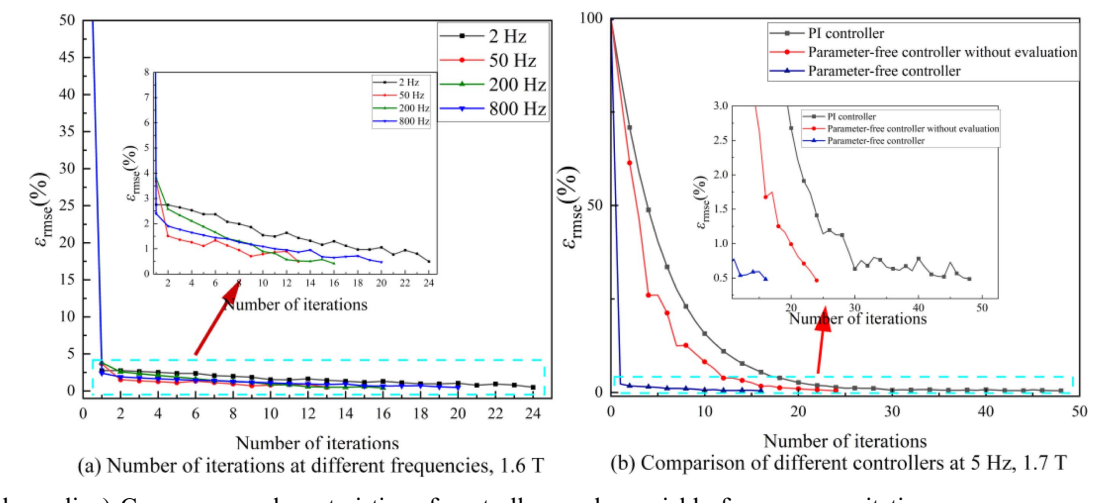


Fig. 7. (Color online) Convergence characteristics of controllers under variable frequency excitation.

as shown in Fig. 7. Fig. 7(a) demonstrates that during the initial waveform estimation phase, the proposed method can effectively reduce the $\varepsilon_{\rm rmse}$ to under 4%. The convergence rate exhibits a strong frequency dependence: at the standard 50 Hz frequency, the error converges to below 0.5% after approximately 10 iterations. In contrast, under 2 Hz low-frequency and 800 Hz high-frequency excitation, due to the strong nonlinear effects of the grain-oriented silicon steel, the convergence process requires about 20 iterations. The error curve demonstrates minimal oscillations and satisfactory stability throughout the convergence process.

As illustrated in Fig. 7(b), the proposed initial waveform estimation mechanism reduces the waveform error during initial operation to 2.3%, representing a significant improvement over traditional controllers. After the iterative optimization involving amplitude adjustment and harmonic suppression, the $\varepsilon_{\rm rmse}$ of the waveform is further reduced to below 0.5%. Even when omitting the initial waveform estimation phase, the polynomial fitting-derived control coefficients achieve a 50% faster convergence rate than empirical coefficients in conventional controllers. In addition, traditional controllers heavily rely on parameter settings, which often lead to overshoot and oscillation in the regulation waveform due to improper settings. Furthermore, the parameters required for different materials vary significantly, greatly increasing the control difficulty.

4.2. Evaluation and analysis of the controller's accuracy

As illustrated in Fig. 8(a), the distortion of the induced voltage waveform measured from induction coils exhibits

distinct harmonic components under varying magnetic flux densities. This phenomenon is mechanistically attributed to odd-order harmonic effects caused by the nonlinear magnetization states of ferromagnetic materials. With increasing magnetic flux density, the third- and fifth-order harmonic components become increasingly prominent, resulting in significant alterations to the original sinusoidal waveform. Such harmonic enhancement produces distinct waveform distortion in the detected signals. The magnetic flux density waveform is similarly affected and distorted, enlarging the hysteresis loop area, as depicted in Fig. 8(b). Upon the implementation of control, the harmonics present in the waveform are processed by the controller within the frequency domain to ensure that the waveform is primarily composed of the fundamental component.

Figure 9 presents experimental data for grain-oriented silicon steel sheets acquired by the measurement system, demonstrating a significant expansion of the hysteresis loop area with increasing excitation frequency. By comparing the waveforms of B(t) and H(t) at 2 Hz and 2000 Hz, it is observed that under low-frequency conditions, a single magnetization cycle is prolonged to 0.5 seconds. This significantly extends the experimental time due to multiple magnetization cycles and data acquisition requirements, which becomes unacceptable in specific measurements. In contrast, under high-frequency conditions, the Joule heating effect between the specimen and the excitation coil is significantly enhanced, resulting in specimen heating. As magnetic losses exhibit a pronounced temperature dependence, a gradual reduction in magnetic losses is observed with increasing temperature,

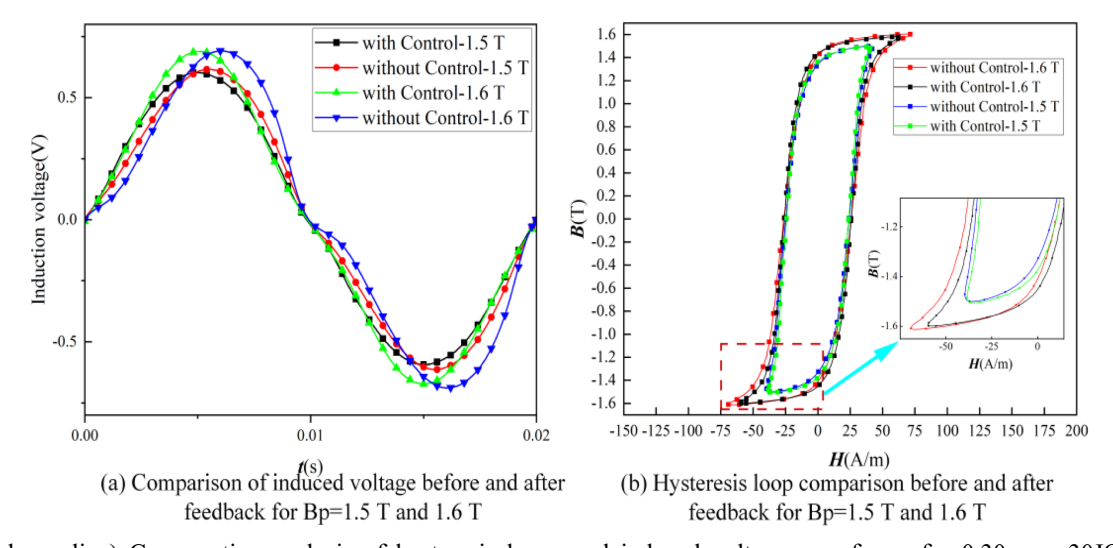


Fig. 8. (Color online) Comparative analysis of hysteresis loops and induced voltage waveforms for 0.30 mm 30JQ130 grain-oriented silicon steel under 50 Hz sinusoidal excitation.

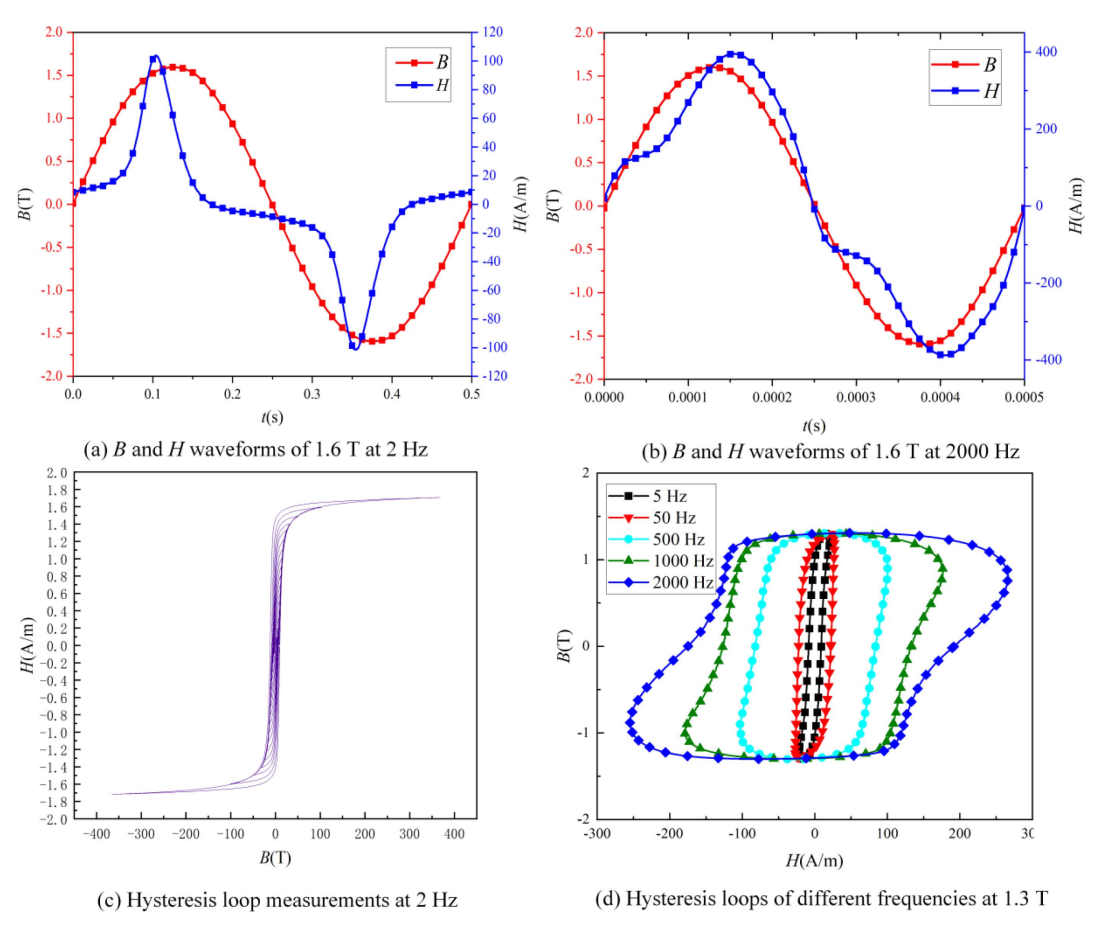


Fig. 9. (Color online) Hysteresis loops and B and H waveform measurements at different frequencies and magnetic flux densities.

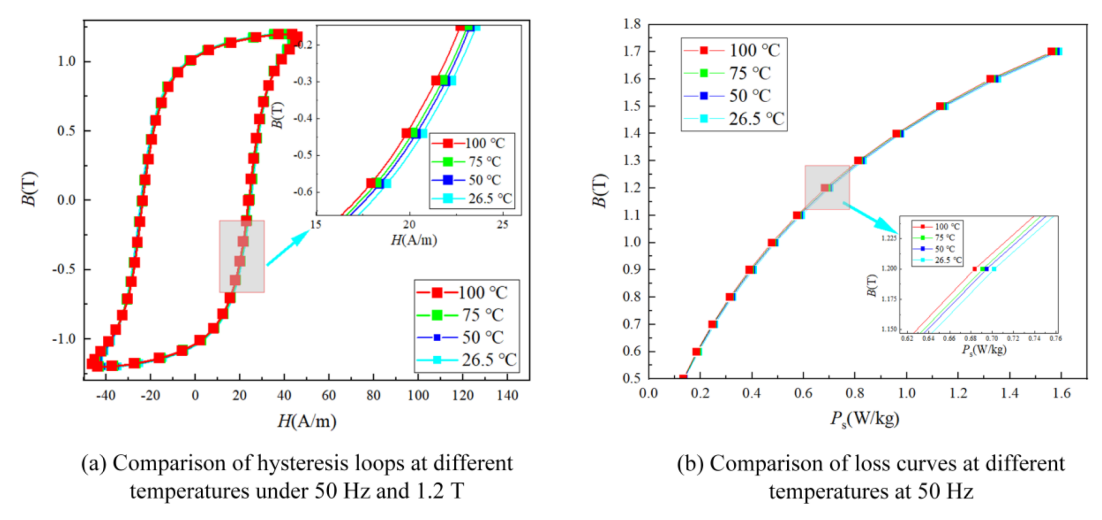


Fig. 10. (Color online) Experimental results on the temperature dependence of grain-oriented silicon steel (B30P105) at 50 Hz.

as is evidenced by the experimental data in Fig. 10. Temperature elevation may introduce additional measurement errors, consequently compromising both the accuracy and repeatability of the experimental results. Thus, accelerating the measurement process is essential

for low-frequency and high-frequency measurements, as it ensures experimental efficiency while maintaining data accuracy and reliability.

To demonstrate the harmonic suppression capability of the proposed algorithm, Fig. 11(a) compares control

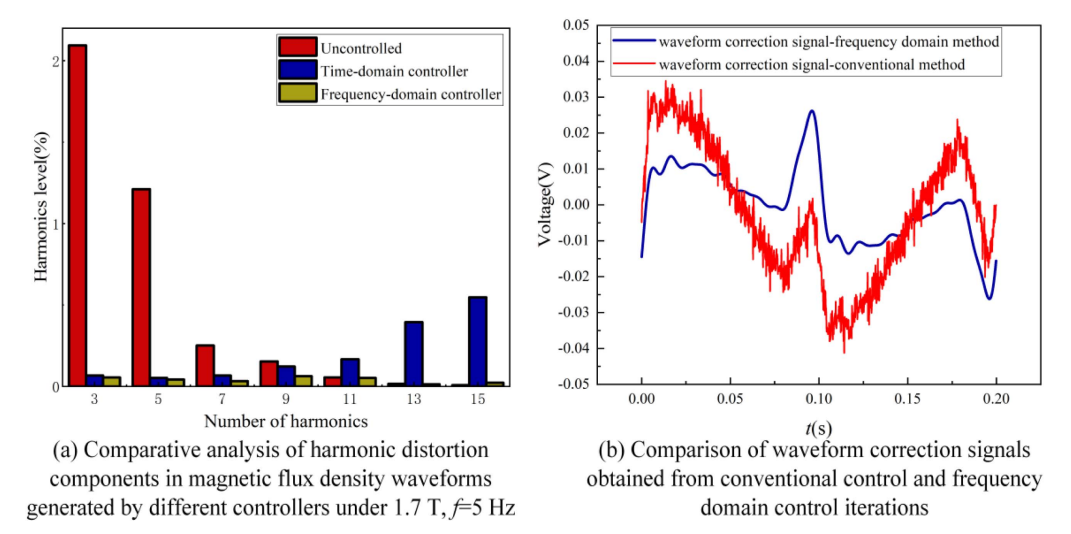


Fig. 11. (Color online) Comparative evaluation of time-domain and frequency-domain control strategies for magnetic property characterization under low-frequency excitation.

performance between the proposed algorithm and the traditional time-domain method under conditions of 1.7 T and 5 Hz. It is observed that the proposed algorithm attains substantial harmonic suppression. Specifically, the harmonic content is reduced from approximately 5% to 0.214%, which is significantly below the control requirement of 0.5%. This effect is primarily attributed to the advantages of frequency-domain methods in waveform regulation. During the feedback control process, the frequency-domain methodology enables the selective omission of higher-order harmonics and implements targeted suppression of corresponding harmonic components, thereby preventing noise from being introduced into the control signal. In contrast, traditional timedomain methods, which utilize waveform subtraction for tracking the target waveform, inevitably introduce measurement noise. By comparing the iterative update waveforms in Fig. 11(b), it is evident that the excitation voltage signals used for waveform correction in the timedomain method contain significantly more noise than those in the frequency-domain method.

To evaluate the measurement uncertainty, the Type A evaluation method was adopted in this study [22]. By performing repeated measurements of the loss, the standard deviation could be represented as:

$$\delta P_{s} = \sqrt{\frac{1}{n-1} \cdot \sum_{i=1}^{n} \left(P_{\text{ave}} - P_{s}^{(i)} \right)^{2}}$$

$$\tag{17}$$

Where $\delta P_{\rm s}$ is the relative deviation of loss, $P_{\rm ave}$ is the average value of multiple measurements, and $P_{\rm s}^{[i]}$ is the measured loss value of the *i*th time. Where $P_{\rm s}$ can be

expressed as:

$$P_{\rm s} = \frac{1}{\rho T} \int_{T} H \cdot \frac{\mathrm{d}B}{\mathrm{d}t} \mathrm{d}t \tag{18}$$

Where ρ is the material density, T is the measurement period. Subsequently, the standard deviation was transformed into the standard error of the mean:

$$\delta_{SEM} = \frac{\delta p_{\rm s}}{\sqrt{n}} \tag{19}$$

As shown in Fig. 12, the losses and uncertainties corresponding to different magnetic flux densities are

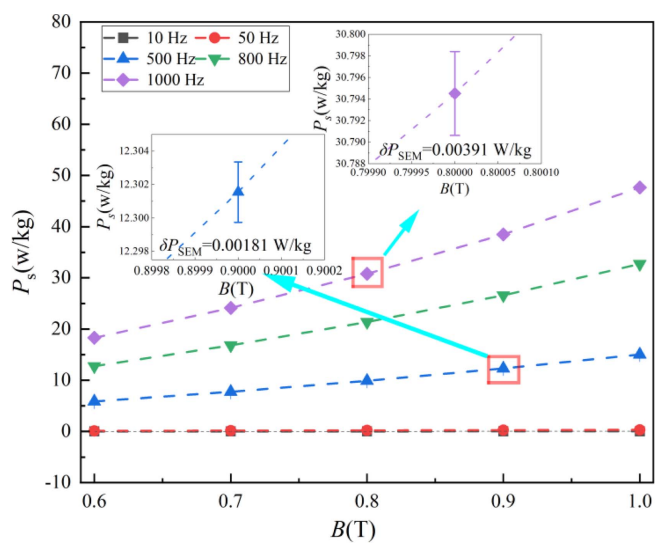


Fig. 12. (Color online) Measurement and uncertainty analysis of silicon steel magnetic properties at different frequencies.

Table 2. Quantitative analysis of the mean and uncertainty of losses at different frequencies.

Different frequencies (Hz)	Uncertainty of measurement loss (W/kg)	Average value of loss (W/kg)
10	0.000070	0.02746
50	0.000333	0.32272
500	0.0018	15.03138
800	0.0053	32.69878
1000	0.0083	47.66181

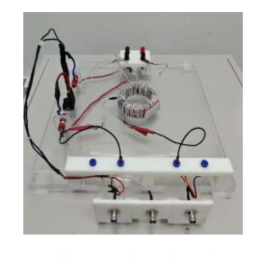
presented under the frequency conditions of 10 Hz, 50 Hz, 500 Hz, 800 Hz, and 1000 Hz. As evident from the figure, the associated measurement uncertainties remain low. The uncertainty values for the specific measurement points are 0.0039 W/kg and 0.0018 W/kg, respectively. Furthermore, the uncertainties of the loss measurements for different frequencies at B_p =1 T are shown in detail in Table 2. These results demonstrate that the maximum loss uncertainty remains below 0.009 W/kg, indicating that the measurement system exhibits high repeatability.

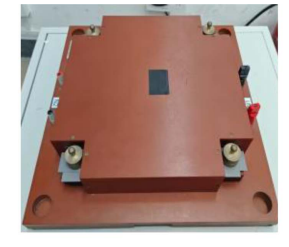
4.3. Evaluation and analysis of controller universality

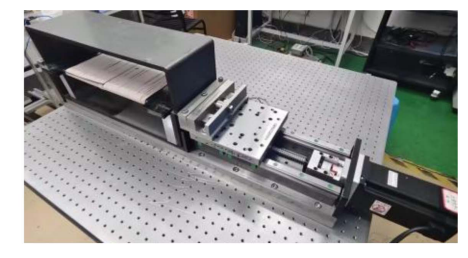
Systematic investigations were conducted on oriented silicon steel specimens under varying magnetic flux density conditions using different testers to evaluate the controller's robustness across different testers. Fig. 13 presents diagrams of the various measurement devices employed, while Table 3 enumerates the number of iterations required for different devices at different frequencies and magnetic flux densities. In the linear region, only a limited number of iterations are necessary to satisfy the requirements, and no significant disparity in the number of iterations is observed between 0.9 T and 1.2 T due to evaluation effects. However, a greater number of adjustments is required in the nonlinear region to minimize the deviation from the target value. As indicated in Table 3, the iteration count is elevated at both low and high frequency extremes. Nevertheless, it remains below 20 in the majority of cases. The waveform shape factor (η_{nrmse}) remains below 0.5% in the final iteration at 1.5 T. The controller exhibits good versatility and has been successfully implemented in experiments with various testers.

5. Conclusion

In this paper, an improved parameter-free waveform controller for measuring the magnetic properties of electrical steels has been proposed. The obtained results indicate that in magnetic properties measurements conducted under low-frequency conditions (5 Hz, Bp=1.7 T), the initial excitation voltage waveform evaluated through







(a) Ring Core Sample

(b) Epstein frame

(c) Single Sheet Tester

Fig. 13. (Color online) Different types of magnetic property measuring testers.

Table 3. Illustration of the number of iterations with different testers.

Measurement	Frequency	Number of iterations		itions	W. C. 1. C. 4. () 415 T
apparatus		0.9 T	1.2 T	1.5 T	Waveform shape factor(η_{nrmse}) at 1.5 T
	2 Hz	8	10	15	0.435215%
EF	5 Hz	5	6	12	0.48255%
	50 Hz	3	4	9	0.395395%
	10 Hz	6	9	15	0.423358%
RCS	500 Hz	7	8	16	0.454309%
	2000 Hz	10	11	32	0.492864%
CCT	20 Hz	6	7	19	0.332547%
SST	50 Hz	4	5	15	0.293457%

the IRLS method enables rapid waveform control, reducing the iteration error to less than 3% during the first waveform iteration and further reducing the waveform root mean square error to less than 0.5% after approximately 15 iterations. In addition, the proposed algorithm leverages FFT decomposition and adaptive parameter tuning to significantly suppress harmonics through adaptive injection of odd-order components with identical frequency, identical phase, and opposite amplitude, thereby reducing the total harmonic distortion from approximately 5% to 0.2%. Compared to conventional methodologies, the proposed approach demonstrates superior performance in suppressing high-frequency harmonics, thereby enhancing measurement accuracy. Regarding the reproducibility of the experiments, the uncertainty was minimal, with the maximum value not exceeding 0.009 W/kg. The controller's implementation process is simplified by eliminating the requirement for additional parameter settings while maintaining control performance. Finally, the controller demonstrates good adaptability through testing on various testers across different frequency bands.

Acknowledgment

This work was supported by the National Natural Science Foundation of China under Grant No. 52477011 and No.52207012.

References

- [1] X. Zhao, D. Zhang, Z. Ren, K. Shi, and Y. Zhang, J. Magn. Magn. Mater. 597, 172021 (2024).
- [2] P. Zhang, W. Liao, B. Lin, N. Wang, C. Li, J. Zhang, and J. Gao, J. Magn. Magn. Mater. 610, 172583 (2024).
- [3] H. Chen, L. Li, W. Song, L. Wang, and Q. Yang, J. Magn. Magn. Mater. **590**, 171689 (2024).
- [4] X. Zhao, Y. Jiang, Y. Wang, and J. Chen, J. Magn. Magn. Mater. 620, 172873 (2025).
- [5] H. Toda, Y. Oda, M. Kohno, and Y Zaizen, IEEE Trans.

- Magn. 48, 3060 (2012).
- [6] N. Yogal, C. Lehrmann, and M. Henke, IEEE Energy Conversion Congress and Exposition (ECCE), (2021), pp. 4176-4181.
- [7] J. Lavers, P. Biringer, and H. Hollitscher, IEEE Trans. Magn. 13, 1128 (1977).
- [8] Q. Wen, Z. Cheng, S. Liu, X. Tan, Y Chen, and J. Liu, J. Mater. Res. Technol. **33**, 2252 (2024).
- [9] H Kagimoto, D Miyagi, N Takahashi, N Uchida, and K Kawanaka, IEEE Trans. Magn. **46**, 3018 (2010).
- [10] P Fagan, B Ducharne, S Zurek, M Domenjoud, A Skarlatos, L Daniel, and C Reboud, IEEE Trans. Instrum. Meas. 71, 6006113 (2022).
- [11] G. Bertotti, E. Ferrara, F. Fiorillo, and M. Pasquale, J. Appl. Phys. **73**, 5375 (1993).
- [12] P. Sankaran, V. Kumar, IEEE Trans. Magn. 19, 1572 (1983).
- [13] T. Todaka, Takeru Sato, S. Ishikawa, Y. Maeda, and M. Enokizono, Mater. Sci. Forum. 670, 327 (2011).
- [14] S. White, T. Krause, and L. Clapham, Meas. Sci. Technol. 18, 3501 (2007).
- [15] A. T. Vo, M. Fassenet, A. Kedous-Lebouc, F. Blache, C. Boudinet, and M.-P. Vaillant, IEEE Trans. Ind. Electron. 67, 9841 (2019).
- [16] S. Zurek, P. Marketos, T. Meydan, and A. J. Moses, IEEE Trans. Magn. 41, 4242 (2005).
- [17] C. Zhang, Y. Li, J. Li, Q. Yang, and J. Zhu, IEEE Trans Ind Electron. **64**, 2476 (2016).
- [18] K. Sumi, Y. Okamoto, K. Fujiwara, and H Sasaki, IEEE 20th Biennial Conference on Electromagnetic Field Computation (CEFC) (2022) pp. 1-2.
- [19] T. Yamaguchi, Y. Kuroda, Y. Okamoto, K. Fujiwara, and H Sasaki, IEEE 21st Biennial Conference on Electromagnetic Field Computation (CEFC) (2024) pp. 1-2.
- [20] T. Nakase, M. Nakano, K. Fujiwara, and N. Takahashi, IEEJ Trans. Fundam. Mater. **119**, 1019 (1999).
- [21] D. Makaveev, J. Maes, and J. Melkebeek, IEEE Trans. Magn. 37, 2740 (2001).
- [22] S. Zurek, Characterisation of Soft Magnetic Materials Under Rotational Magnetisation. CRC Press, Boca Raton, FL (2017) pp. 290-377.